
A Study of Performance Prediction of Natural-Wind Heat Exchangers for Passive Cooling

Anonymous Author(s)

Affiliation

Address

email

Abstract

This paper presents a computationally efficient surrogate-based design framework for natural-wind-driven (fanless) fin–tube heat exchangers, enabling rapid prediction and optimization of thermal–hydraulic performance over a large geometric design space. While natural-wind air cooling offers a promising route to reduce parasitic power in next-generation AI data centers, practical design remains bottlenecked by the high computational cost of resolving complex fin–tube geometries in high-fidelity CFD. To overcome this limitation, we replace the explicit fin–tube core with an equivalent porous-medium representation derived from established correlations, which enables fast 2D porous-zone CFD for scalable dataset generation. Using strategically selected simulation samples, we train Gaussian Process surrogates that accurately approximate heat transfer and pressure-drop behavior across the feasible domain. We then apply Genetic Algorithm optimization on the surrogate predictions to efficiently identify high-performing configurations while minimizing reliance on repeated high-fidelity CFD runs. The proposed workflow is demonstrated under site conditions derived from long-term meteorological observations in Haenam, Korea, supporting rapid and scalable design of passive cooling heat exchangers for large-scale deployments.

1 Introduction

The surge in AI workloads has escalated data center thermal loads, with rack power densities now exceeding 50–100 kW driven by kilowatt-scale GPUs [1]. Scaling conventional active cooling to meet these demands is becoming economically and environmentally unsustainable, highlighting the need for low-parasitic solutions that exploit natural airflow and favorable ambient conditions. Unlike mechanically forced systems, fanless *natural-wind-driven* cooling can reduce operational electricity consumption and infrastructure complexity, making it attractive for large-scale deployments.

Consequently, the demand for natural-wind heat exchangers is rising to meet the industry’s push for cost-effective and sustainable cooling. However, the feasibility and effectiveness of natural-wind cooling are inherently site-dependent: adequate and sufficiently frequent wind availability, combined with moderate ambient temperatures, is required to achieve meaningful heat removal and stable year-round operation. Therefore, identifying locations that satisfy these minimum climatic conditions is a prerequisite for practical deployment.

Haenam County in Jeollanam-do Province presents a compelling candidate site for passive cooling systems due to its coastal microclimate and geographical positioning near the southern edge of the Korean peninsula. The region provides consistent wind patterns, with an annual mean wind velocity of 2.02 m/s and moderate temperatures that average 14.8°C, as recorded by ASOS Station 261 during the observation period of the year [2]. Furthermore, the concurrent development of a

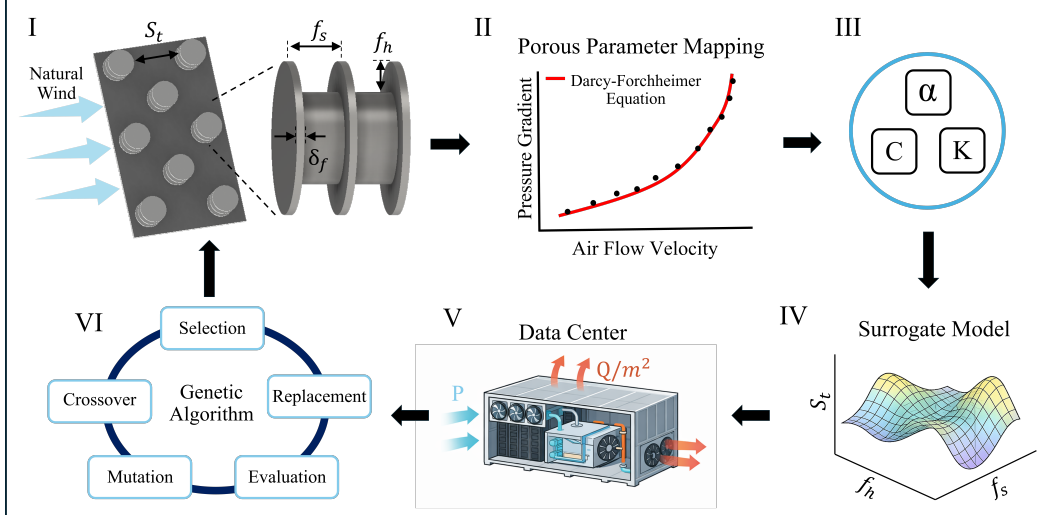


Figure 1: **Schematic overview of the proposed workflow for a fin–tube heat exchanger.** (I) Fin–tube geometry definition (S_t , S_f , δ_f , f_h); (II) unit-cell reduction of the fin–tube array; (III) geometry-to-porous mapping via Darcy–Forchheimer (α , K , C_2); (IV) GP surrogate training using CFD data; (V) GA-based design-space optimization on the surrogate; (VI) system-level evaluation in a modular data-center cooling configuration.

36 national-scale AI computing center initiative strengthens the need for scalable and energy-efficient
37 cooling solutions compatible with domestic climate conditions [3].

38 Despite its promise, the design optimization of natural-wind heat exchangers faces a fundamental
39 computational bottleneck. High-fidelity computational fluid dynamics (CFD) is required to predict
40 performance accurately because the flow and heat transfer are governed by complex phenomena
41 such as wake interactions, mixed convection, and turbulence-enhanced transport in fin–tube arrays.
42 In practice, the design loop is further slowed by the substantial effort required for geometry handling
43 and mesh generation across many candidate configurations. As a result, exhaustive exploration of
44 the continuous design space using full 3D CFD is often infeasible for engineering optimization.

45 In this work, we propose a surrogate-assisted optimization workflow that makes three-dimensional
46 fin–tube cores amenable to fast two-dimensional CFD-based design (Figure 1). Instead of directly
47 simulating the fully resolved 3D fin–tube geometry we introduce an equivalent porous-medium
48 model whose closure coefficients are obtained from newly fitted based on current correlations link-
49 ing fin–tube design parameters to effective flow resistance and heat-transfer performance.

50 This porous reduction enables computationally efficient 2D CFD evaluations that still capture the
51 dominant thermo - hydraulic trends of the original 3D configuration. A Gaussian Process surrogate is
52 trained to approximate the complex design relationships, enabling a Genetic Algorithm to efficiently
53 determine the optimal design solution under constraints, thereby achieving significant computational
54 savings.

55 2 Related Work

56 2.1 Data center free cooling technologies

57 Global hyperscale operators have demonstrated Power Usage Effectiveness (PUE) values below
58 1.15 through strategic free cooling implementations. Meta’s Prineville facility reports PUE 1.09
59 using evaporative cooling and outside-air economizers [4]. Google’s Hamina data center uses Baltic
60 Sea water cooling and reports PUE 1.08 [5]. Microsoft’s Dublin installation employs direct fresh-
61 air cooling with PUE 1.12 [6]. These implementations, however, rely on either consistently cold
62 climates or water-based cooling infrastructure that is not universally available. In Korea, many
63 data centers report higher PUE values (typically 1.3–1.5), and large-scale free cooling deployments
64 remain limited due to humid subtropical summers.

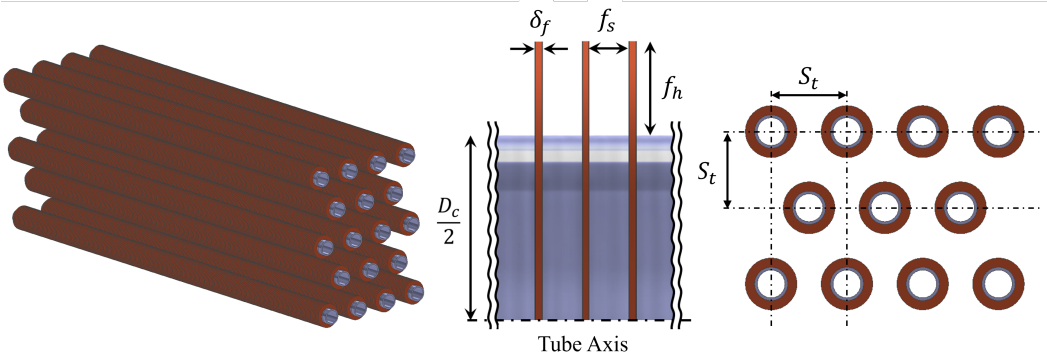


Figure 2: 3D view of the actual fin–tube heat exchanger configuration used in our simulations.

65 2.2 Heat transfer correlations for finned surfaces

66 The thermal–hydraulic characterization of finned tube banks has been extensively studied.
 67 Zukauskas [7] established canonical correlations for crossflow tube banks, often written in the form

$$68 \quad Nu = C_1 Re^m Pr^n \left(\frac{Pr}{Pr_s} \right)^{0.25} \quad (1)$$

68 where the coefficients depend on Re ranges and pitch ratios. For natural convection, Churchill and
 69 Chu [8] proposed correlations relating Nu to Rayleigh number for canonical geometries.

70 Nir [9] developed a friction-factor correlation for staggered annular finned tube banks, expressed as

$$71 \quad f_N = 2.12 Re_{c,f}^{-0.25} W^{-0.55} \left(\frac{D}{d} \right)^{-0.25} K_{c,p} \quad (2)$$

71 where $Re_{c,f}$ is the Reynolds number based on the characteristic fin-collar diameter and maximum
 72 approach velocity, W is a nondimensional fin-spacing parameter, D/d is the relevant diameter ratio
 73 for the tube-fin geometry, and $K_{c,p}$ is a correction factor accounting for tube layout and fin config-
 74 uration. The correlation is typically reported as applicable in the range $Re \approx 3 \times 10^2$ – 10^4 , which is
 75 consistent with the wind-driven operating conditions examined in the present work.

76 2.3 Porous media modeling in CFD

77 The Darcy–Forchheimer equation provides a macroscopic description of flow through porous media
 78 by combining viscous and inertial resistance terms [10]:

$$79 \quad \frac{\Delta P}{L} = \left(\frac{\mu}{K} \right) v + \left(\frac{C_2 \rho}{2} \right) v^2, \quad (3)$$

79 where K is permeability (m^2), C_2 is the Forchheimer (inertial) coefficient (m^{-1}), μ is dynamic
 80 viscosity (Pa·s), ρ is density (kg/m^3), and v is the superficial velocity (m/s). This formulation enables
 81 computational simplification by replacing detailed fin geometry with an equivalent porous zone,
 82 substantially reducing cell numbers while preserving macroscopic thermal–hydraulic behavior [11].

83 2.4 Surrogate modeling and Bayesian optimization

84 Gaussian Process (GP) regression is widely used for surrogate modeling of expensive functions [12].
 85 In addition to point predictions, GP provides uncertainty estimates through posterior variance, en-
 86 abling principled exploration–exploitation trade-offs. Bayesian optimization built on GP surrogates
 87 has shown strong performance in hyperparameter tuning [13], materials design [14], and surrogate-
 88 based optimization [15].

Table 1: Design parameter ranges.

Parameter	Symbol	Range	Unit
Fin height	f_h	[6, 30]	mm
Fin spacing	f_s	[2, 8]	mm
Tube spacing	S_t	[45, 200]	mm
Tube diameter	D_c	24 (fixed)	mm
Fin thickness	δ_f	0.5 (fixed)	mm

Table 2: Porous-medium parameter ranges.

Parameter	Symbol	Range	Unit
Porosity	α	[0.80, 0.941]	–
Viscous resistance	$1/K$	$[8.36 \times 10^3, 1.68 \times 10^5]$	m^{-2}
Inertial resistance	C_2	[0.34, 6.83]	m^{-1}

3 Method

3.1 Parameters

The design space is defined from manufacturing limits, thermal requirements, and the Haenam Sollarseado site conditions. Table 1 summarizes the geometric design space, and Table 2 reports the corresponding porous-medium parameter ranges induced by mapping this design space to an equivalent porous representation. The design parameters (Table 1) are defined in Fig. 1 and explored within the ranges summarized in Table 1.

Geometric Design Parameters. To keep the optimization tractable while preserving the dominant air-side trade-offs under natural wind, we vary fin height (f_h), fin spacing (f_s), and tube pitch (S_t), while fixing the tube diameter (D_c) and fin thickness (δ_f) to standard commercial specifications (Table 1). The selected bounds reflect manufacturable fin geometries and practical clearance against coastal fouling, and the tube-pitch range follows common heat-exchanger layout guidelines that recommend a minimum pitch on the order of $\sim 1.25D$ to ensure mechanical clearance and serviceability.

To ensure physical realizability (i.e., no interference between fins and adjacent tubes), we impose a coupled geometric constraint on h_f :

$$f_h \leq 0.5 \left(\frac{S_t}{\sqrt{2}} - D_c \right) - 0.4 . \quad (4)$$

A 0.4mm offset provides a practical clearance margin against tolerance and discretization-induced interference. This inequality filters out geometries that would collide under the chosen S_t and D_c .

Porous-medium parameters and feasibility. Each fin-tube configuration is represented by an equivalent porous core parameterized by porosity (α), viscous resistance ($1/K$), and inertial resistance (C_2), which are computed from the geometric variables and used in the porous-zone momentum source term of the CFD model. Crucially, the feasible ranges of $(\alpha, 1/K, C_2)$ are not prescribed *a priori*; instead, they are *implied* by the geometric design ranges in Table 1 together with the coupled feasibility constraint in Eq. (4). Applying the geometry-to-porous mapping to all feasible geometries therefore induces the porous-parameter bounds summarized in Table 2.

Sampling for CFD training data. A two-stage LHS strategy is used to construct a compact yet representative CFD training set. We first draw feasible geometries under the coupled constraints (Eq. (4)), map them to $(\alpha, 1/K, C_2)$, and then select CFD cases by LHS in the induced porous-parameter domain to ensure coverage of both boundary and interior regions.

3.2 CFD Simulation

CFD is performed to evaluate the heat transfer rate and pressure drop for the 100 sampled designs and the optimum. The operating condition corresponds to a tube-diameter Reynolds number is $Re = 3,107$ for which wake-induced turbulence is expected. To make large-scale evaluation tractable, the fin-tube core is replaced by an equivalent porous zone and simulated in 2D domain by assuming negligible spanwise gradients. The optimized design is additionally simulated in 3D with the fin geometry explicitly resolved to validate the 2D porous approximation.

Three distinct computational domains were developed:

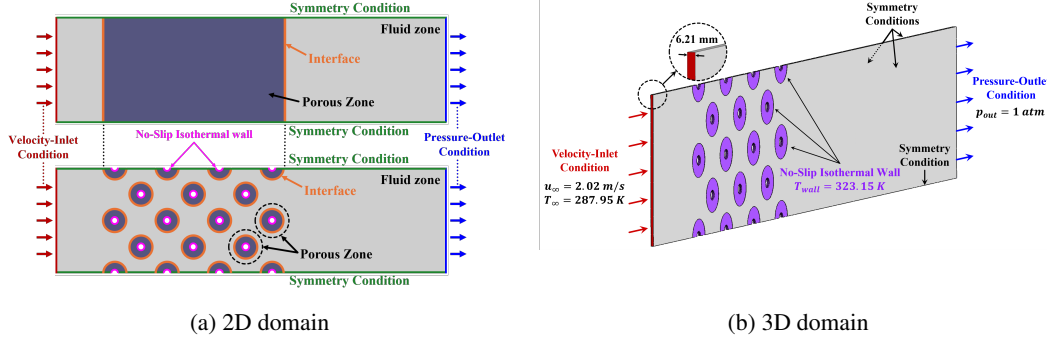


Figure 3: Details of boundary conditions: (a) 2D domain, (b) 3D domain.

Table 3: Mesh configurations for each simulation domain.

Domain	Mesh Type	Number of Cells
2D Pressure Drop Domain	Structured hexahedral	7k
2D Heat Transfer Domain	Unstructured hexahedral	0.15–0.4M
3D High-Fidelity Domain	Unstructured poly-hexcore	35M

- 126 1. 2D Pressure Drop Domain(upper of Fig. 3a): Replaces the fin-tube array with an equivalent
127 porous zone to efficiently predict flow resistance.
128 2. 2D Heat Transfer Domain(lower of Fig. 3a): Incorporates both the porous fin region and
129 the explicit tube wall to account for thermal interaction.
130 3. 3D High-Fidelity Domain(Fig. 3b): Resolves the actual fin geometry (with an axial length
131 set to twice the fin spacing) to validate the simplified models.

132 For the 2D cases, hexahedral meshes were generated using ANSYS Meshing. Structured mesh with
133 an uniform cell size of 10 mm was applied for pressure drop calculations, while a refined resolution
134 of 1 mm was maintained for heat transfer simulations to capture complex flow configurations. The
135 3D simulations utilized an unstructured poly-hexcore mesh generated in ANSYS Fluent Meshing.
136 To ensure accurate heat transfer prediction, the first cell height was set to 0.1 mm, maintaining a non-
137 dimensional wall distance of $y^+ \leq 2$. Final mesh specifications, determined via grid independence
138 tests, are summarized in Table 3. For the two-dimensional heat transfer simulations, the total number
139 of mesh elements varied depending on the fin height and the spacing between fin-tube arrays.

140 In the two-dimensional fluid domain, the continuity, momentum, and energy equations were solved
141 in ANSYS Fluent. The RNG $k-\varepsilon$ turbulence model was selected, as it has been shown to provide
142 improved predictions for separated/curved flows with rotation and enhanced near-wall behavior via
143 its velocity correction [16].

144 Both the fluid zone and the porous zone were modeled using atmospheric dry air, neglecting the ef-
145 fects of humidity. Within the porous zone, flow resistance and thermal behavior were modeled using
146 porous-material properties obtained through the fin-to-porous mapping procedure. Two resistance
147 coefficient and porosity were directly derived from the mapped fin geometry. Since the focus of
148 this study is on the overall pressure drop and the total heat transfer rate as functions of the mapped
149 porous parameters, a thermal equilibrium model was adopted.

150 At the inlet boundary, a constant velocity and temperature was imposed. An atmospheric pres-
151 sure was applied at the outlet boundary condition. On the tube walls, a no-slip boundary condition
152 was enforced, and an isothermal wall condition was applied for a constant temperature of 50 °C,
153 corresponding to the assumed condenser temperature. This value reflects the operating conditions
154 of air-cooled chillers for data-center applications, operating under the Integrated Part Load Value
155 (IPLV) rating condition, which assumes condensation under ambient air temperatures of approx-
156 imately 35 °C. Symmetry boundary conditions were applied at the two boundaries in the spanwise
157 direction. The interfaces between the fluid zone and the porous zone were defined. The initial con-

Table 4: Boundary conditions for each computational domain.

Fluid domain	Location	Details of boundary conditions
All domains	Inlet	$U_\infty = 2.02 \text{ m/s}$, $T_\infty = 287.95 \text{ K}$
	Outlet	$p = 1 \text{ atm}$
	Symmetry	Zero normal velocity and zero normal flux
Except 2D pressure-drop domain	Wall	No-slip condition; Isothermal wall (50°C)
Except 3D high-fidelity domain	Interface	Fluid–porous zone interface

158 ditions for the flow field were set equal to the inlet boundary condition. Details of all boundary and
159 initial conditions are provided in Figure 3 and Table 4.

160 The convergence tolerance was set to $1e-6$ for all CFD simulations. All calculations were contin-
161 ued until the residuals of the continuity, x- and y-momentum, energy, turbulent kinetic energy, and
162 dissipation rate equations satisfied the specified convergence thresholds.

163 All CFD simulations were performed on two high-performance workstations equipped with AMD
164 EPYC 7763 processors (64 cores each) and 512 GB of RAM.

165 3.3 Porous Media Modeling

166 **Geometry-to-Porous Mapping** Each feasible geometry is mapped to an equivalent porous
167 medium characterized by porosity (α), viscous resistance ($1/K$), and inertial resistance (C_2). The
168 finned-array friction factor is modeled by a modified Nir-type correlation:

$$f_N = 1.1 \text{Re}_{D_c}^{-0.25} \left(\frac{S_1}{D_c} \right)^{0.6} \text{AR}^{0.15}, \quad (5)$$

169 where Re_{D_c} is based on D_c and the maximum velocity, S_1/D_c is the transverse pitch ratio, and
170 $\text{AR} = A_{\text{total}}/A_{\text{bare}}$ is the area ratio. We employ this modified form because the original Nir corre-
171 lation is recommended for relatively tight tube spacing (e.g., $S_1/D_c < 2.8$) [9], whereas our natural-
172 wind design space spans $S_1 \in [45, 200] \text{ mm}$ with fixed $D_c = 24 \text{ mm}$, i.e., $S_1/D_c \in [1.88, 8.33]$.
173 To retain accuracy over this wider-pitch regime, we recalibrated the pitch dependence by replacing
174 the original $(S_1/D_c)^{-0.4}$ term with $(S_1/D_c)^{0.6}$, which yields agreement within $\pm 15\%$ against our
175 high-fidelity reference data across the feasible domain.

176 The porosity of the finned array is

$$\alpha = 1 - \frac{\delta_f}{f_s + \delta_f}, \quad (6)$$

177 and the resistance coefficients ($1/K$, C_2) are derived within the Nir framework [9]. For each de-
178 sign point, $1/K$ and C_2 are obtained from a multi-point least-squares fit of the Darcy–Forchheimer
179 relation over $v \in [0.5, 3.5] \text{ m/s}$, representative of local natural-wind conditions. Consequently,
180 the porous-parameter ranges reported in Table 2 are fully induced by the geometric bounds and the
181 physical constraint in Eq. (4), rather than being chosen ad hoc.

182 3.4 Gaussian Process Surrogate Construction

183 To construct the surrogate model $f(\mathbf{x})$ mapping the design vector \mathbf{x} to the performance met-
184 rrics $\mathbf{y} = [Q'', \Delta P]^\top$, Gaussian Process (GP) regression was adopted, defined as $f(\mathbf{x}) \sim$
185 $\mathcal{GP}(m(\mathbf{x}), k(\mathbf{x}, \mathbf{x}'))$. Here, $m(\mathbf{x})$ is the mean function and $k(\mathbf{x}, \mathbf{x}')$ denotes the covariance ker-
186 nel function, which are optimized independently for each target variable.

187 To capture the complex physical characteristics of thermo-hydraulic performance, a competitive
188 selection framework was implemented to compare four kernel architectures: (1) Matérn 5/2 for non-
189 smooth physical transitions, (2) Radial Basis Function (RBF) for smooth variations, (3) Rational
190 Quadratic for multi-scale variations, and (4) a composite kernel ($k_{\text{comp}} = k_{\text{lin}} + k_{\text{nonlin}}$) combin-
191 ing linear trends with non-linear variations. The composite kernel, identified as optimal via cross-
192 validation (R^2), suggests that the performance exhibits a global linear trend dominated by geometric
193 scaling superimposed with local non-linear variations due to flow separation and turbulence.

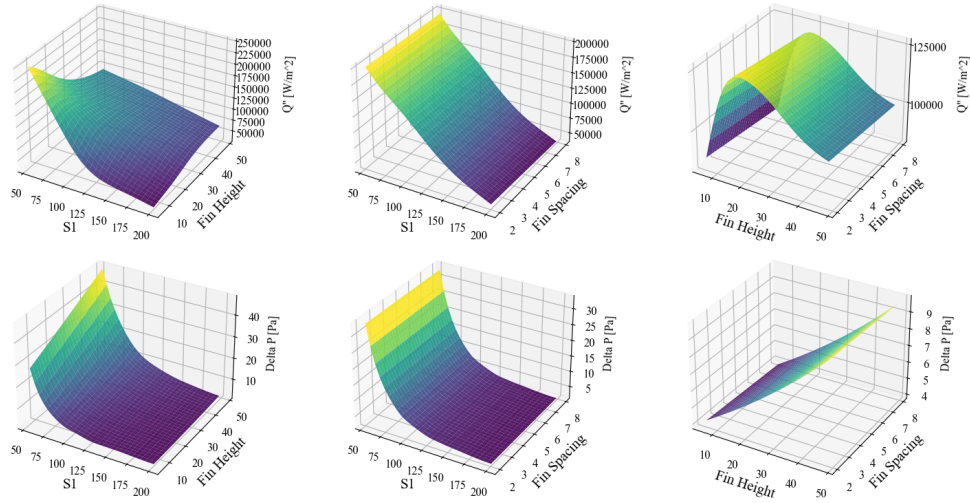


Figure 4: GP response surfaces over pairwise planes in the design space.

194 3.5 Optimization via Uncertainty-Aware Genetic Algorithm

195 Global design optimization is performed by integrating the trained GP surrogate with a Genetic
 196 Algorithm (GA). The surrogate provides the predictive mean (μ) and standard deviation (σ) for both
 197 total heat-transfer rate (Q) and pressure drop (ΔP), which are used to construct the GA fitness. In
 198 this work, the optimization target is defined in terms of heat flux, Q'' , computed by normalizing
 199 the predicted total heat-transfer rate by the porous-zone frontal area indicated in Fig. 3a i.e., $Q'' =$
 200 Q/A_p , where A_p denotes the porous-zone area.

201 Two fitness formulations are considered to account for surrogate uncertainty. In the mean optimiza-
 202 tion mode, the GA maximizes the nominal ratio $\mu_{Q''}/\mu_{\Delta P}$. In the conservative mode (default), the
 203 GA maximizes an uncertainty-adjusted objective that penalizes optimistic heat-flux estimates and
 204 inflatedly rewards underestimated pressure drop:

$$J(\mathbf{x}) = \frac{\mu_{Q''}(\mathbf{x}) - \sigma_{Q''}(\mathbf{x})}{\mu_{\Delta P}(\mathbf{x}) + \sigma_{\Delta P}(\mathbf{x})}. \quad (7)$$

205 This conservative formulation prevents excessive performance overestimation in sparse regions of
 206 the design space and guides the search toward robust optimal designs.

207 4 Results

208 4.1 Gaussian Process Surrogate Performance

209 The surrogate models demonstrate high predictive accuracy for both target responses—heat flux
 210 (Q'') and pressure drop (P). For the heat flux (Q'') model, the surrogate achieves $R^2 = 0.987$,
 211 NRMSE=3.85%, and MAPE=3.1%. For the pressure drop (P) model, the performance metrics are
 212 $R^2 = 0.999$, NRMSE=0.91%, and MAPE=1.7%.

213 These values indicate that both surrogates are sufficiently accurate for design-space exploration
 214 and downstream optimization. The higher fidelity observed for P is consistent with the fact that
 215 pressure loss tends to be governed by comparatively direct geometric-flow resistance relationships.
 216 In contrast, Q'' reflects more complex thermo-fluid interactions (e.g., local boundary layer behavior,
 217 heat transfer enhancement mechanisms) that can introduce stronger nonlinearity and local variation.

218 4.2 Sensitivity and Optimization Results

219 4.2.1 Sensitivity analysis

220 Figure 4 summarizes sensitivity trends inferred from the trained surrogate behavior.

221 The surface gradients indicate that for Q'' , the dominant contributions arise from S_1 and f_h , while
 222 f_s has a comparatively minor effect. In the case of P , the response is strongly dominated by S_1 ,
 223 with secondary contributions from f_h and negligible dependence on f_s .
 224 The visualization confirms that regions yielding high Q'' are not necessarily aligned with regions
 225 minimizing P , motivating the use of ratio-based objectives and global search rather than purely
 226 monotone local tuning. In addition, the surfaces provide interpretability by revealing how the opti-
 227 mum is situated within a broader feasible basin rather than at an isolated spike—consistent with the
 228 stability implied by the conservative objective value.
 229 These results are substantiated by fundamental thermofluid mechanics. The transverse pitch S_1
 230 strictly governs the blockage ratio, wake interference, and bulk flow redistribution, thereby acting as
 231 the primary determinant of pressure drop.
 232 Conversely, the heat transfer performance (quantified by Q'') is inherently driven by the effective
 233 surface area and fin efficiency, which provides a definitive physical explanation for the dominant
 234 influence of fin height f_h .

235 4.2.2 Surrogate-based global optimization

236 Using the GP surrogate as a fast evaluator inside a Genetic Algorithm (GA), the optimization con-
 237 verges to the optimal geometric parameters and predicted performance values shown in Table 5a and
 Table 5b.

Table 5: Predicted optimum design and performance from the surrogate model.

(a) Predicted optimum design variables			(b) Predicted performance variables	
S_1 [mm]	f_h	f_s	Q'' [W/m ²]	ΔP [Pa]
181.0394	28.9923	2.6038	70549.88 ± 3693.96	2.4274 ± 0.3319

238
 239 In particular, the conservative ratio remaining close to the mean ratio indicates that the predicted
 240 optimum is not dominated by excessive surrogate variance.

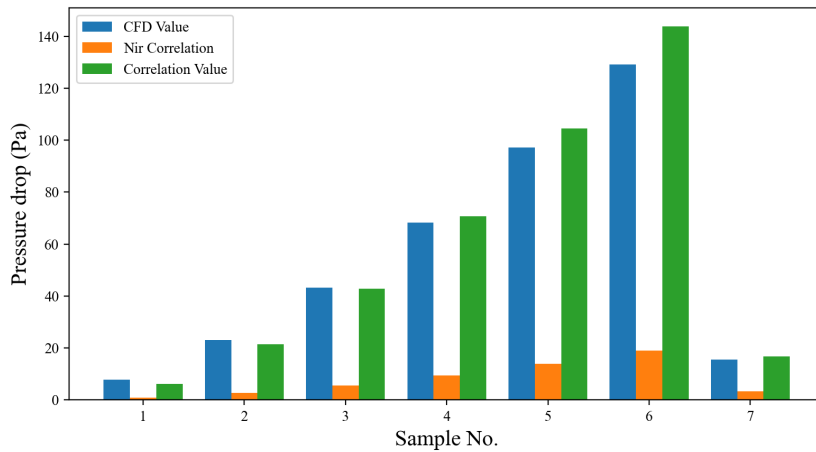


Figure 5: Pressure-drop validation of correlation models

Table 6: Error metrics for pressure-drop prediction relative to CFD (7 samples).

Model	MAE [Pa]	RMSE [Pa]	MAPE [%]	R^2
Nir correlation	47.00	59.19	85.6	-0.980
Modified correlation (Eq. (5))	4.22	6.35	8.4	0.977

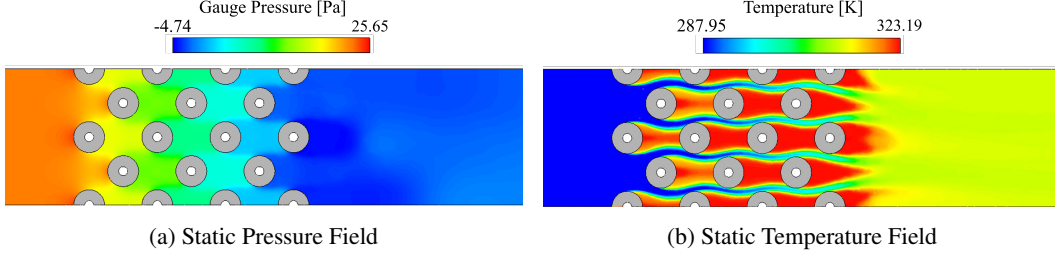


Figure 6: 3D CFD results(mid-span of tube): (a) Static Pressure Field, (b) Static Temperature Field.

Table 7: Comparisons between surrogate prediction and 3D optimal designs and relative errors.

Metric	Surrogate Prediction	3D CFD Value	Error [%]
Heat flux Q'' [W/m ²]	70549.88	56064.55	25.84
Pressure drop ΔP [Pa]	24.29665	23.1146	5.11387

241 4.3 Validation

242 4.3.1 Correlation Validation

243 To justify the modified friction-factor correlation in Eq. (5), we validate its pressure-drop prediction
 244 against high-fidelity CFD results. Figure 5 compares the sample-wise pressure drop ΔP from CFD,
 245 the original Nir correlation, and the proposed modified correlation.

246 Quantitatively, the original Nir correlation severely underpredicts ΔP with **MAE = 47.00 Pa**,
 247 **RMSE = 59.19 Pa**, and **MAPE = 85.6%** ($R^2 = -0.980$; mean bias = -47.00 Pa). In con-
 248 trast, the modified correlation closely matches CFD with **MAE = 4.22 Pa**, **RMSE = 6.35 Pa**, and
 249 **MAPE = 8.4%** ($R^2 = 0.977$; mean bias = 3.15 Pa), with the maximum absolute error reduced
 250 from **110.01 Pa** (Nir) to **14.66 Pa**. These results confirm that the modified correlation provides a
 251 significantly improved pressure-drop closure for the porous-medium parameterization used in this
 252 study.

253 4.3.2 Prediction Results

254 Table 7 compares the surrogate-based prediction against the 3D CFD result (Fig. 6) at the predicted
 255 optimum. The pressure drop is captured with a small error (5.11%), while the heat flux prediction
 256 shows a moderate deviation (25.84%). Overall, the surrogate provides sufficiently reliable guid-
 257 ance for identifying low- ΔP designs and narrowing down promising candidates for high-fidelity
 258 validation.

259 **Limitations and Future Work** Our dataset generation relies on a 2D porous-medium approxima-
 260 tion and thus does not capture 3D effects from axial fin-tube non-uniformity. We also restrict the
 261 tube-bank layout to a staggered case with equal transverse/longitudinal pitch, excluding in-line and
 262 more general arrangements. Fin thickness is fixed (not optimized). Finally, validation is limited to
 263 CFD; experimental verification with a fabricated prototype remains future work.

264 References

- 265 [1] Arman Shehabi, Sarah Smith, Dale Sartor, et al. United states data center energy usage report.
 266 Technical Report LBNL-1005775, Lawrence Berkeley National Laboratory, 2016.
- 267 [2] Korea Meteorological Administration. Automated synoptic observing system (asos) historical
 268 data: Station 261 (haenam), 2024. Accessed via KMA data portal.
- 269 [3] Samsung SDS. Solarseedo national ai computing center project proposal. Technical report,
 270 Samsung SDS Consortium, 2025. Consortium technical report.

- 271 [4] Meta Platforms, Inc. Prineville data center: Sustainability report. Technical report, Meta
272 Platforms, Inc., 2022.
- 273 [5] Google. Environmental report: Data center efficiency. Technical report, Google, 2023.
- 274 [6] Microsoft. Dublin data center: Design and operations overview. Technical report, Microsoft,
275 2022.
- 276 [7] A. Zukauskas. Heat transfer from tubes in crossflow. In *Advances in Heat Transfer*, volume 8,
277 pages 93–160. Academic Press, 1972.
- 278 [8] S. W. Churchill and H. H. S. Chu. Correlating equations for laminar and turbulent free convec-
279 tion from a vertical plate. *International Journal of Heat and Mass Transfer*, 18(11):1323–1329,
280 1975.
- 281 [9] A. Nir. Heat transfer and friction factor correlations for crossflow over staggered finned tube
282 banks. *Heat Transfer Engineering*, 12(1):43–58, 1991.
- 283 [10] M. Kaviany. *Principles of Heat Transfer in Porous Media*. Springer-Verlag, 2 edition, 1995.
- 284 [11] K. Boomsma, D. Poulikakos, and F. Zwick. Metal foams as compact high performance heat
285 exchangers. *Mechanics of Materials*, 35(12):1161–1176, 2003.
- 286 [12] Carl Edward Rasmussen and Christopher K. I. Williams. *Gaussian Processes for Machine
287 Learning*. MIT Press, 2006.
- 288 [13] Jasper Snoek, Hugo Larochelle, and Ryan P. Adams. Practical bayesian optimization of ma-
289 chine learning algorithms. In *Advances in Neural Information Processing Systems*, 2012.
- 290 [14] Peter I. Frazier. A tutorial on bayesian optimization. arXiv preprint arXiv:1807.02811, 2018.
- 291 [15] Kalyanmoy Deb, Amrit Pratap, Sameer Agarwal, and T. Meyarivan. A fast and elitist multiob-
292 jective genetic algorithm: NSGA-II. *IEEE Transactions on Evolutionary Computation*, 6(2):
293 182–197, 2002.
- 294 [16] Talha Bin Nadeem, Muhammad Imran, Adeel Arshad, and Emad Tandis. Parametric study
295 and design optimization of finned tube heat exchangers for enhanced indirect evaporative
296 cooling. *Thermal Science and Engineering Progress*, 69:104481, January 2026. doi:
297 10.1016/j.tsep.2026.104481.

298 **AI Co-Scientist Challenge Korea Paper Checklist**

299 **1. Claims**

300 Question: Do the main claims made in the abstract and introduction accurately reflect the
301 paper's contributions and scope?

302 Answer: Yes

303 Justification: The abstract and introduction clearly claim a rapid design framework enabled
304 by porous-medium approximation. These claims are substantiated by our results, where we
305 identified and verified the underlying thermal-hydraulic correlations through rigorous CFD
306 analysis, demonstrating high predictive fidelity and computational acceleration.

307 **2. Limitations**

308 Question: Does the paper discuss the limitations of the work performed by the authors?

309 Answer: Yes

310 Justification: We explicitly discuss the inherent trade-offs of the 2D porous-medium ap-
311 proximation, acknowledging that it does not fully capture complex three-dimensional flow
312 features. We also address the reliance on empirical correlations and manage surrogate un-
313 certainty through a conservative optimization objective.

314 **3. Theory Assumptions and Proofs**

315 Question: For each theoretical result, does the paper provide the full set of assumptions and
316 a complete (and correct) proof?

317 Answer: Yes

318 Justification: We explicitly state the assumption that the complex 3D geometry can be
319 approximated by a 2D porous medium. We provide a proof of this assumption's validity
320 by rigorously validating the 2D model against full 3D CFD simulations, demonstrating that
321 the approximation holds with high accuracy.

322 Guidelines:

323 4. Experimental Result Reproducibility

324 Question: Does the paper fully disclose all the information needed to reproduce the main
325 experimental results of the paper to the extent that it affects the main claims and/or conclu-
326 sions of the paper (regardless of whether the code and data are provided or not)?

327 Answer: Yes

328 Justification: We provide the full governing equations and define the geometric design
329 space. Furthermore, we provide the complete source code for CFD reproduction and data
330 sampling, ensuring that the experimental results and the optimization workflow can be fully
331 reproduced.

332 5. Open access to data and code

333 Question: Does the paper provide open access to the data and code, with sufficient instruc-
334 tions to faithfully reproduce the main experimental results, as described in supplemental
335 material?

336 Answer: Yes

337 Justification: We provide the complete source code and datasets as anonymized supple-
338 mental material. This includes the CFD case files for data generation, the Python scripts
339 for Gaussian Process training and Genetic Algorithm optimization.

340 6. Experimental Setting/Details

341 Question: Does the paper specify all the training and test details (e.g., data splits, hyper-
342 parameters, how they were chosen, type of optimizer, etc.) necessary to understand the
343 results?

344 Answer: Yes

345 Justification: In the context of our numerical experiments, we specify the Latin Hyper-
346 cube Sampling (LHS) method for CFD-based dataset generation and define the explicit
347 boundaries of the design space. Key modeling choices for the Gaussian Process and Ge-
348 netic Algorithm are described in the paper, with full configuration details provided in the
349 supplemental code.

350 7. Experiment Statistical Significance

351 Question: Does the paper report error bars suitably and correctly defined or other appropri-
352 ate information about the statistical significance of the experiments?

353 Answer: Yes

354 Justification: We quantitatively report the statistical performance of the surrogate models
355 using error metrics such as R^2 , NRMSE, and MAPE. Furthermore, we explicitly utilize the
356 predictive standard deviation (σ) derived from the Gaussian Process posterior to quantify
357 uncertainty and construct confidence-aware objective functions for optimization.

358 8. Experiments Compute Resources

359 Question: For each experiment, does the paper provide sufficient information on the com-
360 puter resources (type of compute workers, memory, time of execution) needed to reproduce
361 the experiments?

362 Answer: Yes

363 Justification: We provide details regarding the computing resources (e.g., CPU specifi-
364 cations, RAM) and the average wall-clock time required for both the CFD data generation and
365 the surrogate model training/optimization process in the Supplemental Material, allowing
366 for an estimation of the total computational cost.

367 **9. Code Of Ethics**

368 Question: Does the research conducted in the paper conform, in every respect, with the
369 NeurIPS Code of Ethics <https://nips.cc/public/EthicsGuidelines>?

370 Answer: Yes

371 Justification: We have carefully reviewed the NeurIPS Code of Ethics and confirm that our
372 research conforms to it in every respect. Our work focuses on numerical simulations for
373 energy-efficient engineering design and does not involve human subjects or sensitive data.

374 **10. Broader Impacts**

375 Question: Does the paper discuss both potential positive societal impacts and negative
376 societal impacts of the work performed?

377 Answer: Yes

378 Justification: We explicitly discuss the broader positive societal implications of our work,
379 focusing on the critical need for sustainable infrastructure in the era of large-scale AI.
380 By enabling zero-energy cooling, our framework directly addresses the escalating energy
381 demands and carbon footprint of data centers, aligning with global sustainability goals and
382 the transition toward carbon-neutral computing.

383 **11. Safeguards**

384 Question: Does the paper describe safeguards that have been put in place for responsible
385 release of data or models that have a high risk for misuse (e.g., pretrained language models,
386 image generators, or scraped datasets)?

387 Answer: NA

388 Justification: The proposed work focuses on physics-based engineering simulations for
389 heat exchanger design. It does not involve generative AI models (e.g., LLMs, image gener-
390 ators) or scraped datasets that pose high risks for misuse; therefore, specific safeguards for
391 responsible release are not applicable.

392 **12. Licenses for existing assets**

393 Question: Are the creators or original owners of assets (e.g., code, data, models), used in
394 the paper, properly credited and are the license and terms of use explicitly mentioned and
395 properly respected?

396 Answer: Yes

397 Justification: We utilize and properly cite standard open-source Python libraries (e.g.,
398 Scikit-learn, NumPy) for the surrogate modeling and optimization, adhering to their re-
399 spective permissive licenses. The CFD dataset used in this work was generated entirely by
400 the authors, so no external data assets were involved.

401 **13. New Assets**

402 Question: Are new assets introduced in the paper well documented and is the documenta-
403 tion provided alongside the assets?

404 Answer: Yes

405 Justification: We introduce a new CFD simulation dataset and a Python-based optimization
406 codebase. These assets are provided in the anonymized supplemental material, accom-
407 panied by a comprehensive file that documents the directory structure, dependencies, and
408 step-by-step usage instructions.

409 **14. Crowdsourcing and Research with Human Subjects**

410 Question: For crowdsourcing experiments and research with human subjects, does the pa-
411 per include the full text of instructions given to participants and screenshots, if applicable,
412 as well as details about compensation (if any)?

413 Answer: NA

414 Justification: This research is purely computational, involving numerical simulations
415 (CFD) and machine learning optimization. It does not involve any crowdsourcing experi-
416 ments or research with human subjects.

417 **15. Institutional Review Board (IRB) Approvals or Equivalent for Research with Human**
418 **Subjects**

419 Question: Does the paper describe potential risks incurred by study participants, whether
420 such risks were disclosed to the subjects, and whether Institutional Review Board (IRB)
421 approvals (or an equivalent approval/review based on the requirements of your country or
422 institution) were obtained?

423 Answer: NA

424 Justification: The research relies exclusively on numerical simulations (CFD) and compu-
425 tational optimization algorithms. It does not involve any human subjects or participants;
426 hence, IRB approval or risk disclosure is not applicable.